



ORIGINAL RESEARCH ARTICLE

Effect of Rotational Speed on Mechanical, Microstructure, and Residual Stress Behaviour of AA6061-T6 Alloy Joints through Friction Stir Welding

Virendra Pratap Singh, Ashish Kumar, Rajan Kumar, Anchit Modi, Deepak Kumar, Vinyas Mahesh, and Basil Kuriachen

Submitted: 17 May 2023 / Revised: 18 June 2023 / Accepted: 5 July 2023 / Published online: 24 July 2023

In the present work, the behaviour of an AA6061-T6 alloy joint through friction stir welding was studied comprehensively under a set of processing parameters so as to establish a better microstructure-strength relationship in the joint. In-depth investigations have been done on intermetallic compounds and their phases using SEM, XRD, optical microscopy, and EDS, and thereby on the mechanical properties of the welded joint through tensile, hardness, and residual stress. The results revealed the evolution of grain boundaries and the existence of second-phase particles such as Mg_2Si , $MgZn_2$, $MgCu_2$, and Al_2CuMg . Moreover, using a rotational speed of 800 rpm results in enhanced hardness, tensile strength, and flexural strength. The highest and lowest tensile strengths of 198 and 171 MPa correspond to 800 and 600 rpm, respectively. The grain size distribution in the weld zone is 76.94, 0.83 and 36.82 μm for 600, 800, and 1000 rpm, respectively. Flexural strength was improved for the 800-rpm case and reached a maximum of 380 MPa. The lowest residual stress was found for an 800-rpm sample with tensile and compressive nature of stresses. Ductile fracture behaviour was obtained for tensile samples obtained at 600 and 800 rpm, whereas in the case of 1000 rpm, brittle fracture behaviour was seen.

Keywords AA6061-T6 alloy, fracture analysis, friction stir welding, mechanical behaviour, microstructure, residual stress

1. Introduction

The effort involved in producing conventional fusion welding with better strength, fatigue resistance, and corrosion resistance has limited its usage on aluminium alloys of the 6000 series, which are commonly used in pioneering industries like automotive, railways, marine, and construction. Therefore, it is crucial to study welding methods for such materials due to their extensive usage in various industries. Lightweight structures are a significant design element in the aerospace industry, and aluminium alloys are preferred over steel alloys due to their lower density. To weld aluminium alloys, the solid-state friction stir welding (FSW) technique is extensively utilised for materials with high-melting points, such as steel and aluminium alloys (Ref 1, 2). The Welding Institute (TWI) and Cambridge University collaborated to develop the FSW process as a solid-state joining of aluminium alloys (Ref 3). Numerous studies have been conducted so as to enhance the mechanical performance of the joint and address any defects in the FSW process. Researchers have discovered ways to improve the quality of the weld and its mechanical properties (Ref 4, 5). For instance, Kadian and Biswas (Ref 6) studied the material flow behaviour of CuB370 and AA6061 dissimilar plates during FSW and proposed a new model for the material flow of dissimilar materials in FSW that takes into account the strain rate and temperature-dependent material properties.

Liu et al. (Ref 7) conducted a study on the 6061-T6 alloy using the vortex-friction stir welding (VFSW) process. The main focus of their research was to investigate the changes in the microstructure of the alloy during the welding process. The experimenters used microhardness and tensile strength measurements as indicators of microstructural changes and also examined the grain structure and precipitate in different zones.

This invited article is part of a special topical issue of the *Journal of Materials Engineering and Performance* on Residual Stress Analysis: Measurement, Effects, and Control. The issue was organised by Rajan Bhambroo, Tenneco, Inc.; Lesley Frame, University of Connecticut; Andrew Payzant, Oak Ridge National Laboratory; and James Pineault, Proto Manufacturing on behalf of the ASM Residual Stress Technical Committee.

Virendra Pratap Singh, Department of Mechanical Engineering, National Institute of Technology Mizoram, Aizawl 796012, India; and Department of Mechanical Engineering, IES College of Technology, Bhopal 462044, India; **Ashish Kumar**, Department of Mechanical Engineering, Delhi Technological University, Delhi 110042, India; and Department of Mechanical Engineering, Galgotias College of Engineering and Technology, Greater Noida 201310, India; **Rajan Kumar**, Department of Mechanical Engineering, IES College of Technology, Bhopal 462044, India; **Anchit Modi**, Department of Basic Sciences, IITM, IES University, Bhopal 462044, India; **Deepak Kumar**, Department of Mechanical Engineering, Carnegie Mellon University, Pittsburgh, PA 15213; **Vinyas Mahesh**, Department of Mechanical Engineering, National Institute of Technology, Silchar, Assam 788010, India; and Department of Engineering, City, University of London, London, UK; and **Basil Kuriachen**, Department of Mechanical Engineering, National Institute of Technology Mizoram, Aizawl 796012, India; and Department of Mechanical Engineering, National Institute of Technology Calicut, Kerala 673601, India. Contact e-mail: virendraps07@gmail.com.

The results indicated that the heat-affected zone (HAZ) was the weakest region of the VFSW joint. The weakening in the HAZ was primarily due to the enlargement of particles in the structure of tiny materials. In the nugget zone of the weld (WNZ), there was continuous and dynamic rebuilding of crystals, but it was not enough due to the self-adjusting nature of plastic deformation in the VFSW process. Solid solution strengthening occurred in the WNZ at high temperatures during the VFSW process, leading to a higher microhardness value compared to the HAZ.

Kalinenko et al. (Ref 8) conducted an experiment to explore the consequences of temperature during FSW, the microstructure of aluminium-alloy 6061 joints created by FSW, and their ability to withstand high temperatures. They used a finite-element modelling (FEM) approach to understand the microstructural data and quantified the temperature distributions generated during FSW. The researchers found that the microstructure in the stir zone was susceptible to abnormal grain growth after heat treatment, which occurred rapidly when heating after welding from room temperature to solution temperature. Humphrey's cellular-growth model described the annealing behaviour in all welded conditions. In situations with low heat input, the final grain size was small due to competition between normal grain growth and abnormal grain growth, which was caused by a combination of a fine-grain microstructure and a low volume fraction of second-phase particles. Conversely, high-heat input conditions produced a relatively coarse grain structure and a high-volume fraction of particles in the stir zone, providing microstructural stability.

Choi et al. (Ref 9) examined how linear friction welding (LFW) can strengthen AA7075-T6 alloy joints. They used LFW to join two pieces of AA7075-T6 alloy and conducted experiments to study the microstructure and mechanical properties of the welded joint. They found that the LFW process caused dynamic recrystallization and resulted in a refined microstructure with improved mechanical properties. The authors identified that the strengthening mechanism of the joint was due to the creation of nanoscale strengthening precipitates, such as MgZn₂ and Mg₂Si, during the welding process (Ref 10, 11). In contrast, Tavassolimanesh and Alavi Nia (Ref 12) proposed a novel method for manufacturing bimetallic tubes using the FSW process, where they created bi-tubes from aluminium and copper alloy. They discovered that as the rotational speed increased, the joint strength decreased, and one of the significant issues after welding is the creation of residual stress in construction. The welding process produces both mechanical and thermal residual stresses in the joint and its surroundings, which depend on the yield strength of the parent metal and the local temperature. It becomes crucial to study and calculate the residual stresses on the mechanical performances of welded sensitive structures, such as pressure vessels. Sometimes, when there are residual stresses, they can cause notable changes in the shape of an object through plastic deformation, resulting in warping and distortion (Ref 13).

Several techniques have been utilised to calculate the residual stresses, including slitting (Ref 14, 15), contour (Ref 16, 17), and hole drilling technique (Ref 18, 19). Marek et al. (Ref 20) and Hamilton et al. (Ref 21) described how the longitudinal residual stress distribution of an improved cast Al-alloy, AlSi9Mg, was affected by different parameters used in friction stir processing (FSP). They obtained residual stress through the material flow model in FSPed AlMg9Si by taking the material flow behaviour into consideration during welding

(Ref 21). Furthermore, they examined the impact of FSP constraints on residual stress in an improved cast Al-alloy, AlSi9Mg (Ref 22), and studied the influence of modified FSP on residual stress in the same alloy (Ref 23). Their findings suggest that an increase in tool rotational speed leads to an increase in residual stress. Additionally, compared to the retreating side, residual stresses are greater on the advancing side. Moreover, Alinaghian et al. (Ref 24) explored the use of ultrasonic vibrations to measure residual stress in aluminium AA6061-T6 after FSW. Using high-frequency vibrations can suppress the residual stress up to 45% and also enhance the weld strength. They also found that using ultrasonically assisted FSW (UAFSW) can reduce welding forces compared to conventional FSW.

Donne et al. (Ref 25) utilised x-ray, neutron diffraction, and synchrotron methods to evaluate the residual stresses and found a better outcome in all three cases. Transverse stresses were lower than longitudinal stresses, and residual stress distribution was analogous on both lower and upper weldment surfaces. The residual stress value obtained was 20-50% of the yield strength of the parent material, depending on the linear and rotational speeds and tool pin diameter. Ma et al. (Ref 26) utilised the FSW on an AA2024 to investigate the remaining stresses present in the material during mechanical drawing. They were able to effectively diminish these stresses in the weld region. The key to achieving a successful weld was the management of various process parameters, such as linear speed, rotational speed, tool shape, and penetration. As far as the author's knowledge goes, there is no clear report on the microstructural, mechanical, and XRD-based residual stress distribution of AA6061-T6 subjected to friction stir welding. Therefore, in this research work, the dispersion of residual stress and mechanical properties of an AA6061-T6 alloy joint through FSW were investigated, with a focus on three different rotational speeds at constant welding speeds.

2. Experimental Method

The aluminium AA6061-T6 plate of dimension 120 × 60 × 4 mm is used to carry out the experiment. The representation of the FSW procedure and tool dimension is shown in Fig. 1(a) and (b). The chemical composition of the plate material is mentioned in Table 1. Before performing the experiment, plate surfaces were properly cleaned with a microbrush and then with acetone. An H13 tool steel is used for an FSW taper cylindrical threaded tool with a shoulder diameter of 18 mm and a pin length of 3.8 mm. The metallographic and other mechanical testing samples were cut using a CNC wire EDM (model Elektra, Maxicut 523). The metallographic samples were polished with emery sandpaper and then, etched with Keller's reagent to obtain the microstructural characteristics of the joints. The microstructures were seen through an optical microscope (model Leica DMI500M) and scanning electron microscopy (SEM) (model Zeiss Supra 40) built into the EDX system. X-ray diffraction (XRD) was used to analyse the microstructure and phases. The microhardness values were taken transverse to the welding direction of joints in a 1 mm space with a 100 g loading force and a dwell time of 10 s. Tensile tests and 3-point bending tests were done with the help of a UTM (Model: Instron, 8862) with 1 mm/min of crosshead speed. Both face bends and root bends were tested to

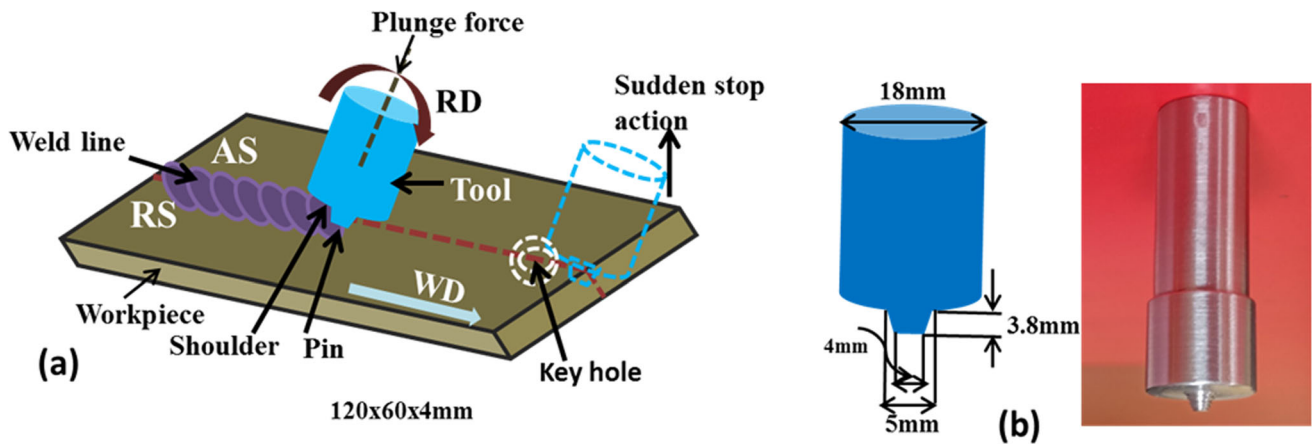


Fig. 1 Representation of (a) FSW process and (b) FSW tool

Table 1 Chemical composition of AA6061-T6 alloy, wt.%

Al	Mg	Si	Ti	Cr	Mn	Fe	Cu	Zn
Bal.	0.976	0.563	0.01885	0.1101	0.08	0.528	0.48	0.111

Table 2 Types of samples and process parameters

Sample	Plunge depth/Tilt angle	Traverse speed, mm/min	Rotational speed, rpm	Revolutionary Pitch, mm/rev
W-A1	0.1/2°	50	600	0.083
W-A2			800	0.063
W-A3			1000	0.050

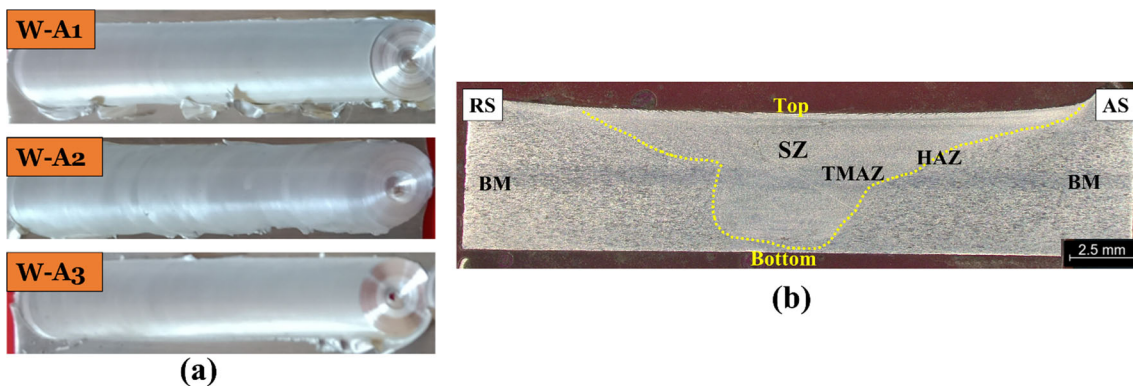


Fig. 2 (a) Weld appearance and (b) macrostructure of welded part showing SZ, TMAZ, and HAZ

identify the flexural strength and mode of failure. The XRD-based residual stress distribution of AA6061-T6 subjected to FSW was calculated both in the longitudinal and transverse directions. Fracture analysis of tensile fracture samples was performed with the help of FE-SEM. There were three different sets of rotational speeds, and a constant transverse speed was taken, as shown in Table 2, where the revolutionary pitch is the ratio of rotational to transverse speed. In all cases, the tilt angle was kept at 2° forward and the plunge depth at 0.1 mm. Revolutionary pitch is the ratio of traverse speed to rotational speed (mm/rev).

3. Results and Discussion

3.1 Microstructure Analysis

The weld appearance of the joint surface at all three sets of parameters is shown in Fig. 2(a). For samples W-A1 and W-A3, a lot of weld flash is seen due to inadequate heat input. Whereas, for sample W-A1, no flashes are seen. Figure 2(b) shows the macrostructure of the FSW joint, identifying the SZ, TMAZ, and HAZ. EDS mapping of base metal (AA6061-T6) is shown in Fig. 3. Magnesium and silicon are the two major

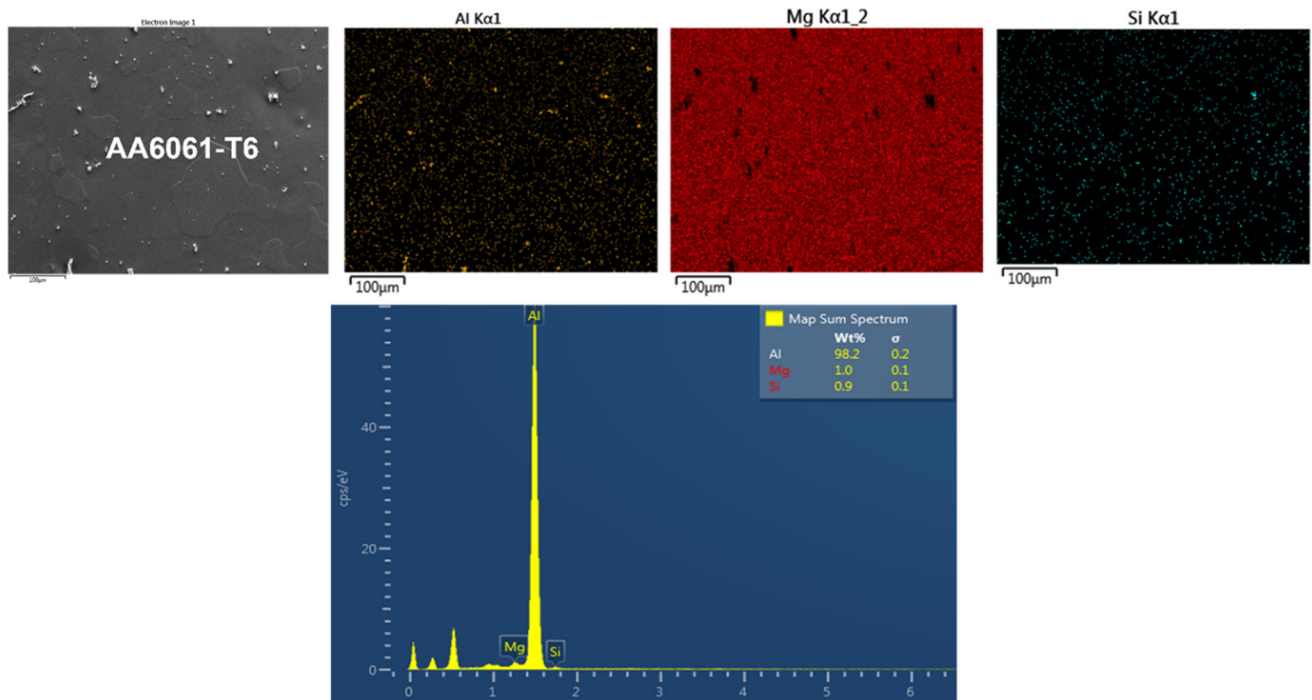


Fig. 3 EDS mapping of base metal (AA6061-T6)

alloying elements present and play an important role in bonding during welding. To validate the above statements, XRD analysis of the weld has been accomplished. Figure 4(a), (b), and (c) confirms that a huge fraction of intermetallic compounds (IMCs) such as Mg_2Si , $MgZn_2$, $MgCu_2$, and Al_2CuMg formation takes place. The high-magnification optical images of all sets of welded samples have been shown in Fig. 5, 6 and 7. Three distinct zones were displayed individually, i.e. HAZ, TMAZ, and SZ, in each case. No volumetric defects were found in any of the weld samples. As the heat input increases by increasing the rotational speed, grain size distribution is severely affected, as shown in Fig. 8(a), (b), and (c). During low-heat input (W-A1), very coarse grains with an average grain size of $76.94 \mu m$ were seen (as referred to in Fig. 8a). Whereas, in the case of W-A2, an average grain size of $0.83 \mu m$ was observed due to the proper material mixing and adequate heat generation in this case (as referred to in Fig. 8b). Very high and very low heat input leads to improper material intermixing, reducing the strength of the joint (Ref 27). Fine grain was observed in the TMAZ section of the weld compared to SZ in the case of W-A1, whilst elongated grains were observed in HAZ, as shown in Fig. 5(a), (b), and (c).

The unusual grain evolution was attributed to the grain refinement on the top and bottom surfaces of the weldment. The effect of grain refinement is noticeable at the weld surface; therefore, the weakest zone was generated beside grain growth. The microstructural stability in the remaining weld zone leads to abnormal coarse grain growth (Ref 28, 29). Any increment in rotational speed, i.e. sample W-A3, increases the heat input, and due to this, the material flow and stirring action over the weldment are reduced, causing coarser grains (average grain

size $36.82 \mu m$) compared to the W-A2 case and hence, the joint strength (Ref 30).

During welding, a very complex and irregular grain growth behaviour is seen, and it is very tough to plot the exact behaviour and reason of the phenomenon. Whereas, with the help of Humphreys's cellular model, this occurrence has been tried to explain. Such complex occurrences can be seen for high-stacking-fault energy materials like aluminium alloys (Ref 31, 32). The annealing single-phase alloy behaviour is directed by the high-angle boundary (HAB) fraction and its distribution throughout the weldment (Ref 31). Whereas the material holds second-phase particles (i.e. AA6061-T6 alloys), the nature of grain growth is moreover affected by the material's pinning effect, which may be measured by the so-called Z parameter, $Z = 3F_v R/d$, where 'Fv' is the material's volume fraction, 'R' is the average grain size, and "d" is the average size (Ref 32). The fundamental properties of microstructure should be measured within the micrograph. This method can effectively be useful for the uncharacteristic grain growth taking place in FSW, as validated by Hassan et al. (Ref 33).

In the HAZ region, the size of the grain was nearly the same as the base metal grain. These explanations are renowned for the FSW of Al-alloys and are usually ascribed to a distinct rate of recrystallization. The entire documentation can be described with reference to the material flow behaviour prompted by the FSW tool shoulder. It has been described that the moving tool entangles the base metal surface during the welding process and accumulates near the tool pin (Ref 34). The strain rate refers to the change in strain of a material over time. When the strain rate is extremely low, the material's deformation can be viewed as a series of steps, with the material remaining in static equilib-

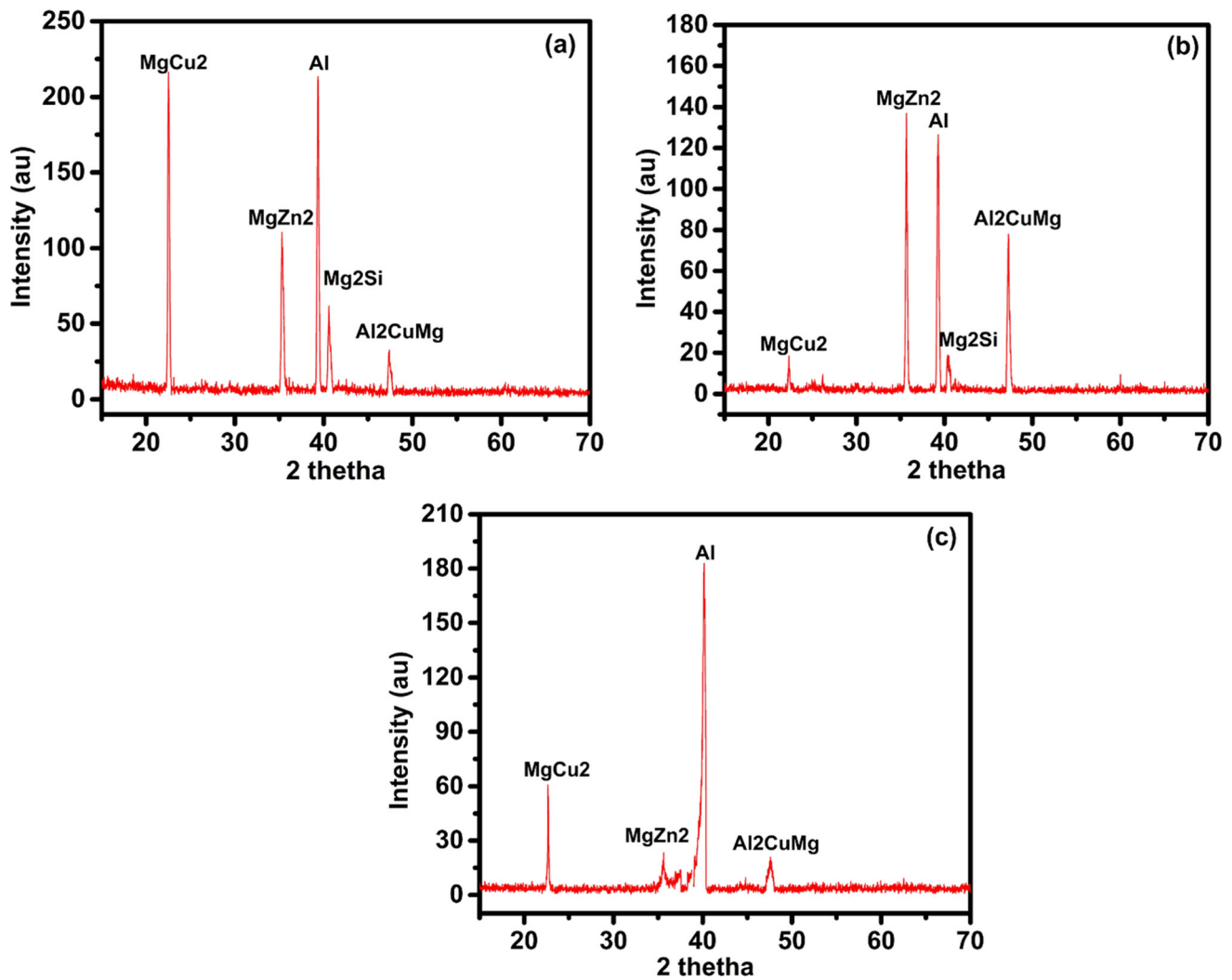


Fig. 4 X-ray diffraction (XRD) of welded samples (a) W-A1, (b) W-A2, and (c) W-A3

rium. In such cases, the process can be regarded as quasi-static, and it can be analysed using the mechanics of materials approach. However, when the strain rate is high, the internal stresses within the material propagate as waves and do not instantaneously transmit throughout the entire material (Ref 35). In FSW, weld grain size and its effect on mechanical properties are mainly dependent on heat input during the process. Heat input varies with rotational speed and, hence, the deformation of the material. In the first case (i.e. W-A1, 600 rpm), heat input is lower at a lower rotational speed, and hence the stirring action is also moderate, and due to this, grain size is coarser (refer to Fig. 8a). Whereas, at higher rotational speed conditions (i.e. W-A3, 1000 rpm), heat input is extremely high, and due to this material sticking, a high-heat gradient takes place, resulting in coarser grain (refer to Fig. 8c). Considering a moderate heat input case (i.e. W-A2, 800 rpm), adequate heat generation and optimum stirring occur, resulting in fine-grain size (refer to Fig. 8b). The heat generation during FSW is mainly from the friction between the tool and the stirred

material, and the heat input during FSW can be calculated using Eq 1 (Ref 36-38).

$$q = \frac{4}{3} \Pi^2 \mu p \omega R^3 \quad (\text{Eq 1})$$

where q is the heat input, p is the pressure, μ is the friction coefficient, R is the radius of the shoulder. And ω is the rotation speed. If the traverse speed is also considered, Eq 2 is obtained.

$$Q = \frac{4}{3} \Pi^2 \mu p \omega R^3 \frac{\alpha \omega}{v} \quad (\text{Eq 2})$$

where Q is the heat input per unit length, α is the heat input efficiency, and v is the traverse speed.

3.2 Mechanical Properties

3.2.1 Tensile Test. Tensile stress vs. tensile strain and true stress vs. true strain graphs are shown in Fig. 9(a) and (b), respectively. The mechanical properties were found to have

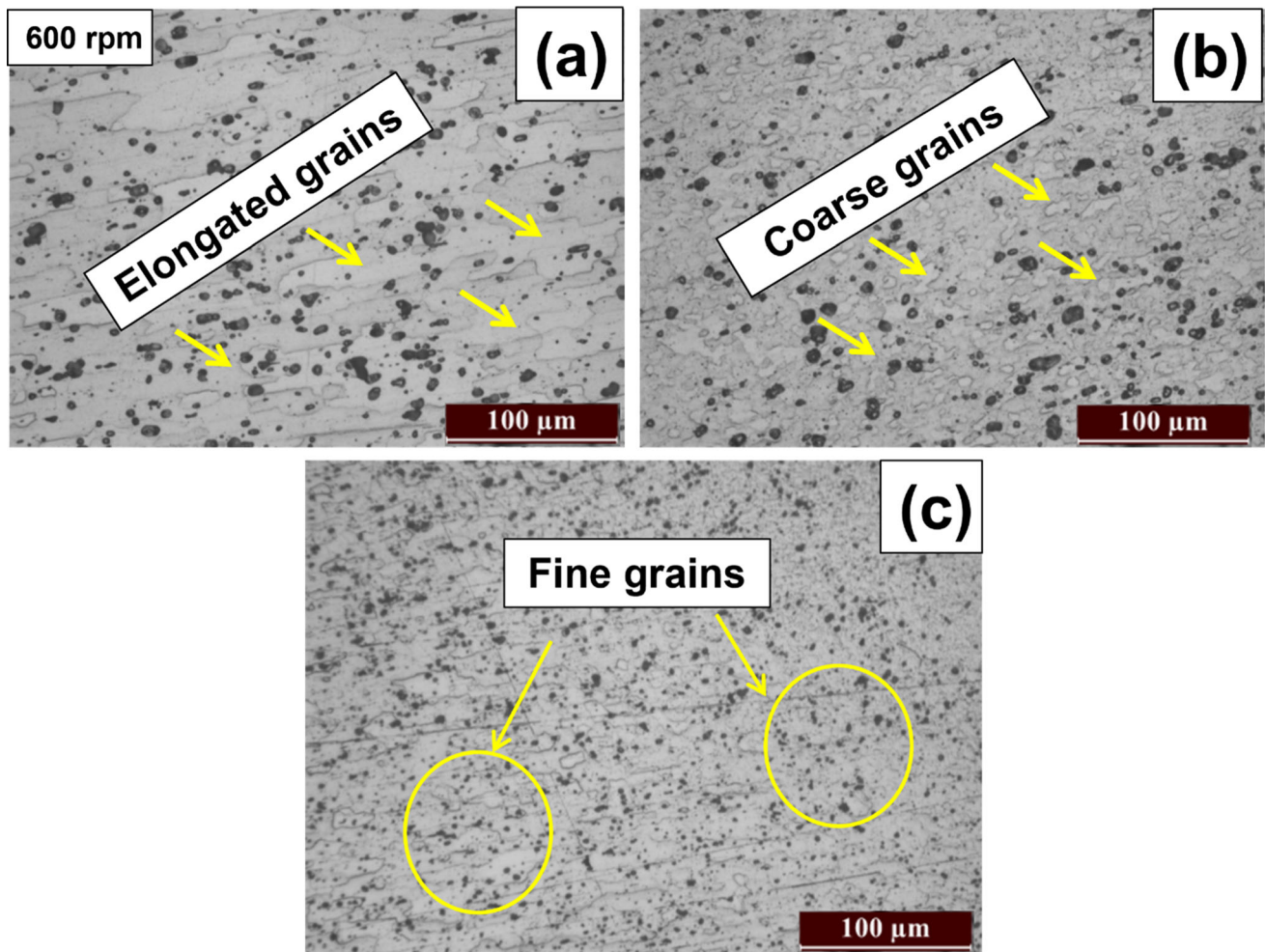


Fig. 5 Optical microstructure of welded sample W-A1: (a) HAZ, (b) SZ, and (c) TMAZ

decreased as a result of the tensile test. The maximum tensile stress for W-A1, W-A2, and W-A3 is 171, 198, and 180 MPa, respectively. A maximum joint efficiency of 84.25% was attained for sample W-A2, whereas a minimum of 72.77% is for sample W-A1, at a lower rotational speed (i.e. at 600 rpm). It has been analysed from Fig. 9 that, with a rise in rotational speed from 600 to 1000 rpm, by keeping welding speed constant, the tensile stress value steadily increased, but at higher speed (i.e. higher heat generation condition), the tensile stress is lower than the moderate heat generation condition, i.e. 800 rpm (W-A2). Proper material mixing and grain refinement are the main causes of increasing tensile strength (Ref 39, 40). When the revolutionary pitch is higher (i.e. 0.083 and 0.063 mm/rev), the tensile strength is lower, but it increases as the revolutionary pitch decreases (i.e. 0.05 mm/rev). The maximum tensile strength is obtained at the lowest revolutionary pitch of 0.05 mm/rev. These results indicate that a softening effect has occurred in the AA6061-T6 due to FSW, just as it did in the other heat-treatable Al-alloys. The softened levels or weld strength of the joints are significantly affected by the

process parameters. The optimum process parameters can be determined from the relationship between the weld properties and the process parameters (Ref 36, 37, 41-43). Too high and too low heat inputs deteriorate the weld strength due to improper material mixing and the high possibility of IMC formation, respectively. At 800 rpm, which is a moderate heat input case as compared to the other two cases, therefore, proper material mixing took place and hence, the strength.

The decrease in mechanical properties during the FSW is caused by the precipitate's dissolution in the metal matrix. This leads to a weakening of the material. After examining various regions of the material following the FSW process, it was discovered that different regions exhibit different stress behaviours. The HAZ region had the least strength due to the precipitate's dissolution and the lack of imminent grain growth. When the plastic strain reaches the point of failure in the HAZ, the nugget area has a strain rate of only 2.3%, resulting in failure occurring in the HAZ (Ref 44, 45). The figure clearly illustrates that the tensile properties of every joint exhibit a lower value compared to the base material. Especially, the elongation of the joint is far lower than that of the base material,

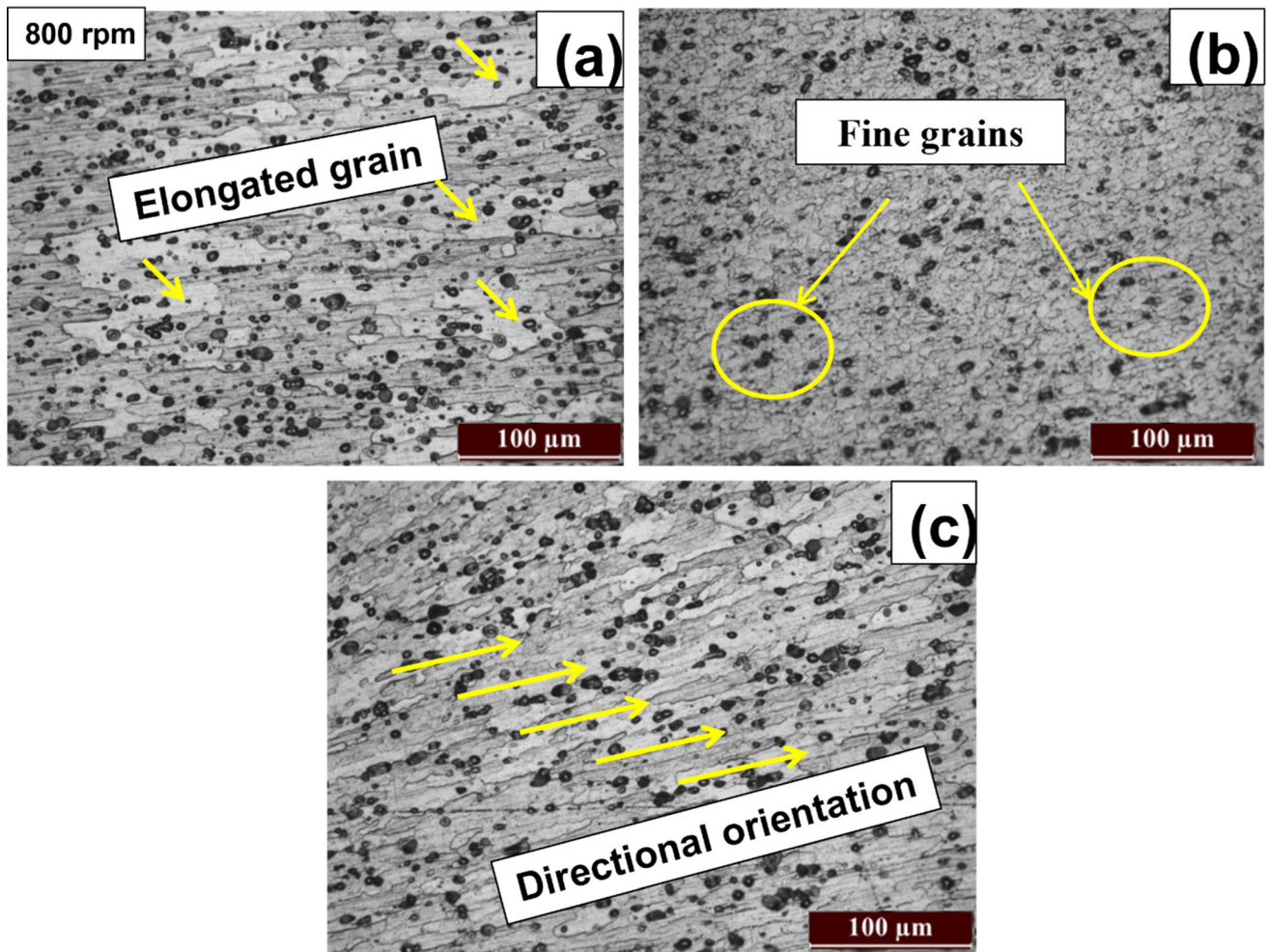


Fig. 6 Optical microstructure of welded sample W-A2: (a) HAZ, (b) SZ, and (c) TMAZ

and its maximum is merely 2%. Intermetallic formation during welding is the main cause of high strength but lower ductility in all three cases, especially for W-A2.

3.2.2 Three-Point Bend Test. In the next step, the three-point bending test has been done. At least two FSW samples were tested for both root bend and face bend. The welded structure had very few surface cracks and noticeable changes in shape due to plastic deformation, as observed through a face-bend test. When the sample experiences compressive stress, the bottommost surface is hard to develop micro-stress concentration, as the AA6061-T6 comes in the face-centred cubic (FCC) family and has a greater number of slip systems and better compatibility of material deformation, and the weld surface did not show any cracks during the bend test (Ref 46, 47). Intermetallic compounds consist of two or more metallic elements. However, unlike typical metals, they exhibit a unique combination of bonding that encompasses metallic, covalent, and ionic characteristics. This distinctive bonding arrangement grants them several advantageous properties, such as reduced

weight, enhanced strength, increased rigidity, and superior resistance to corrosion, especially under elevated temperatures. Nonetheless, their practical applications are restricted due to their inherent brittleness at room temperature (RT). This brittleness poses challenges in the fabrication process and renders them susceptible to fractures (Ref 48). Bending stress is calculated by Eq 3.

$$\sigma = \frac{Mc}{I} \quad (\text{Eq 3})$$

' M ' denotes bending moment, which is obtained by multiplying the given force with the given distance between that point of interest and the force, ' c ' denotes distance from natural axis (NA) (Fig. 10) and ' I ' represents moment of inertia.

The root-bend stress of samples W-A1, W-A2, and W-A3 is 340, 380, and 360 MPa, respectively, as shown in Fig. 11(a), (b), and (c). Whereas, in the case of a face bend, the bending stresses of samples W-A1, W-A2, and W-A3 are 302, 330, and 290 MPa, respectively. In several cases, the rise in strength is

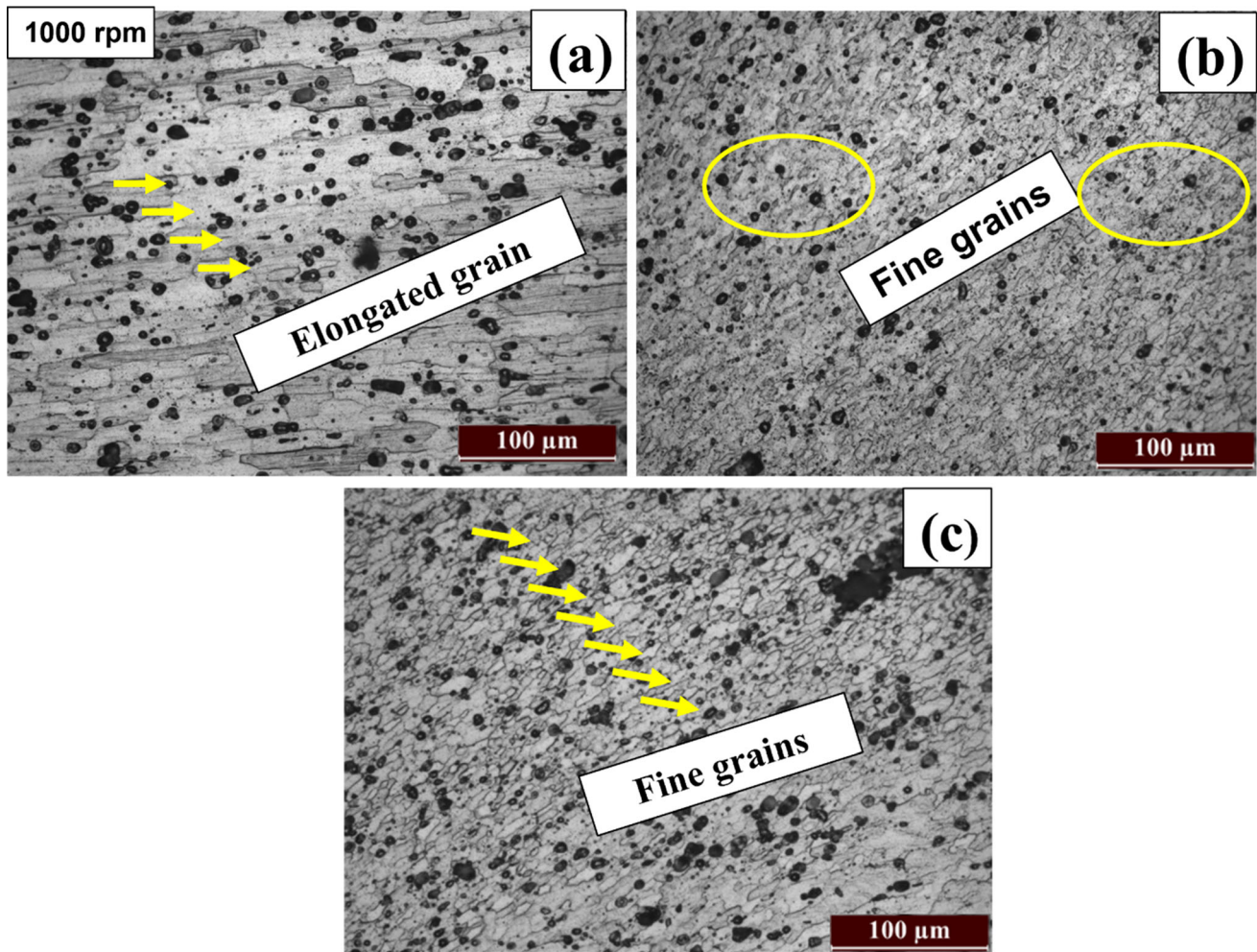


Fig. 7 Optical microstructure of welded sample W-A3: (a) HAZ, (b) SZ, and (c) TMAZ

accompanied by a decrease in ductility. The fine precipitates dispersed homogeneously in the SZ prevent the mobility of dislocations, resulting in a noticeable decrease in ductility. Compared to the base metal, the ductility has decreased in all cases except sample W-A3, i.e. higher heat input conditions. In this case, the ductility of the welding sample touches the base metal ductility in the root-bend case (as shown in Fig. 11c). In the case of W-A2, both face and root-bend ductility are the same, and their strength is also similar, i.e. there is very little variation. This is an indication that appropriate welding occurred under moderate heat conditions. Whereas, in the other two cases, the bend stress (root bend) is much higher than the face-bend stress. The primary factor is having a consistent distribution of grains with no voids in the structure. Also, the formation of clusters of two different precipitate phases that impede the movement of dislocations and the sliding of grain boundaries during the process. The findings indicate that as the hardness of a material increases, its flexural strength generally decreases, which is an acceptable outcome. However, amongst the various samples tested, those rotated at a speed of 800 rpm exhibited higher flexural strength than the others, possibly because this speed led to a maximum hardness of approximately 72 HV. These values suggest that the root side of the

weld was stronger than that of the face-side weld. This could be caused by the fact that the lower side of the weld was exposed to restricted downward movement due to the bed backing plate. The flexural stress values were comparatively higher than the tensile values, and this was due to the higher temperatures involved during FSW (Ref 49).

3.2.3 Microhardness. The microhardness of the welded sample was calculated across the welding line direction. The microhardness curves for the welded sample and base metal are characterised in Fig. 12. Based on the findings on the hardness, it was noted that the reduction in both the retreating and advancing sides of the alloys was comparable for all the parameters. The highest microhardness value of 91 HV was observed for sample W-A3, i.e. high-heat condition. Whilst the maximum microhardness values of 61 HV and 70 HV were obtained for samples W-A1 and W-A2, respectively. The key reason for these microhardness differences is due to the IMC's formation. As described in the literature, small precipitates in AA6061-T6 alloys play a critical role in increasing the mechanical strength (Ref 50-52).

Microhardness values vary on the advancing and retreating sides as well. In all cases, microhardness on the advancing side is higher compared to the retreating side (as shown in Fig. 12).

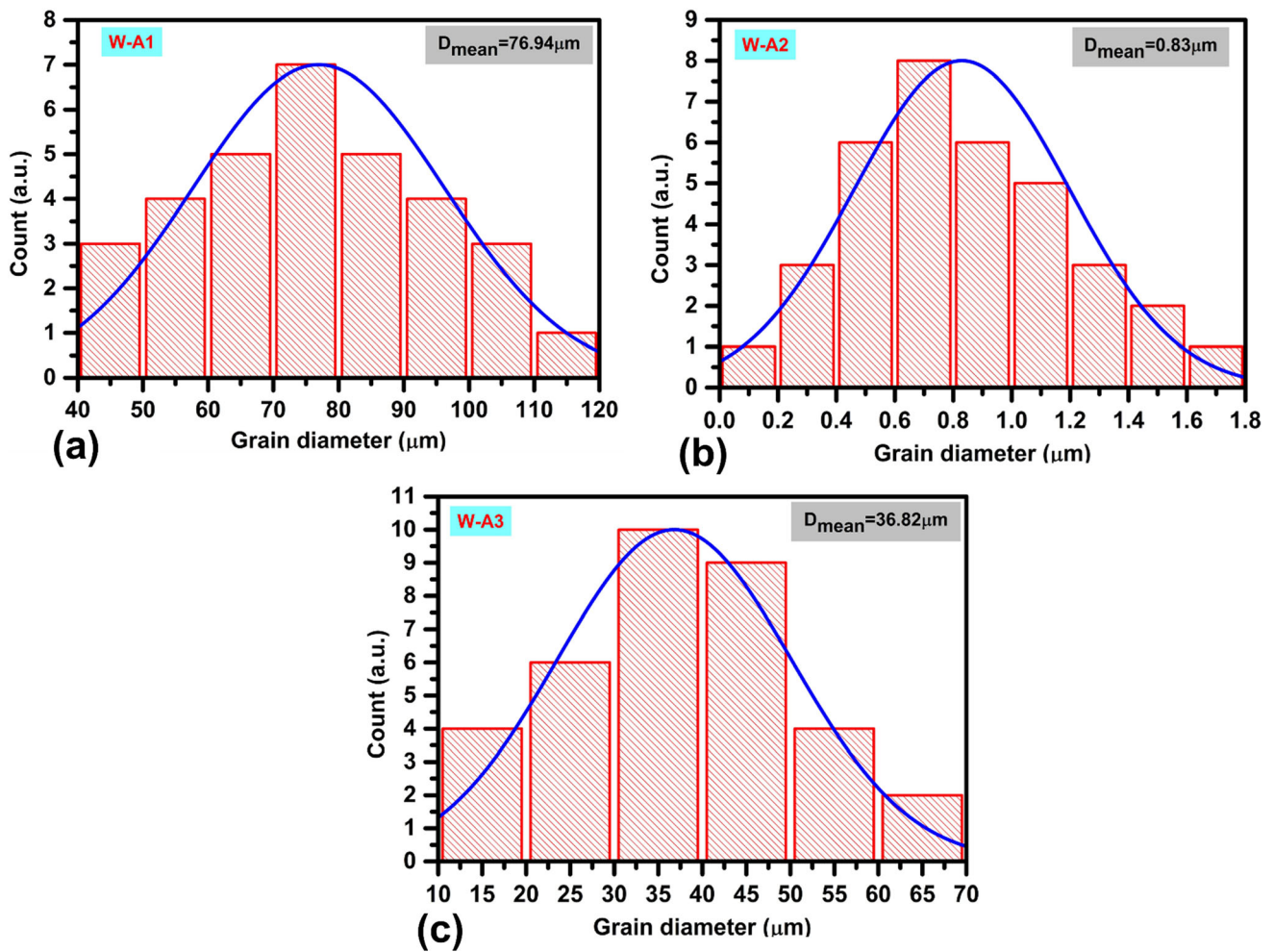


Fig. 8 Grain size distribution of samples: (a) W-A1, (b) W-A2, and (c) W-A3

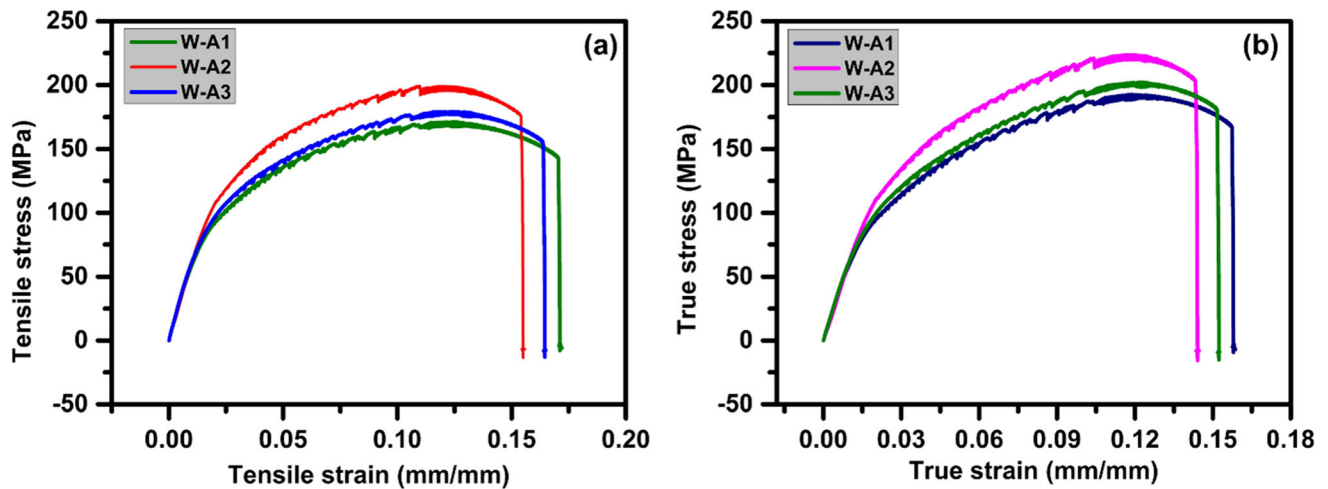


Fig. 9 Tension test of welded samples (a) tensile stress vs. tensile strain curve and (b) true stress vs. true strain curve

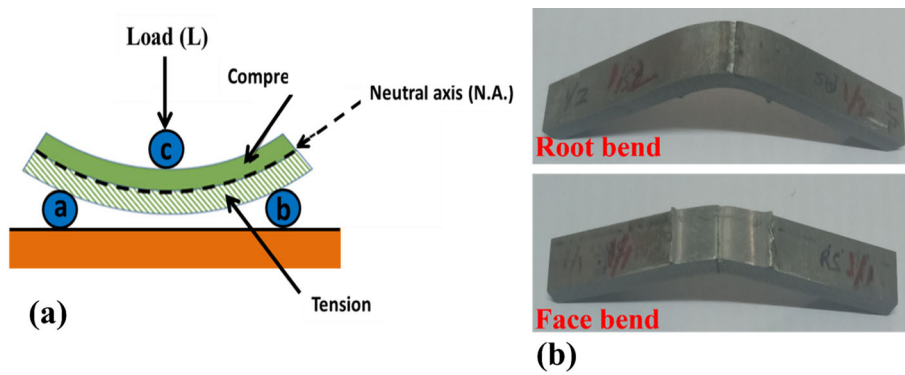


Fig. 10 Schematic diagram of 3-point bending

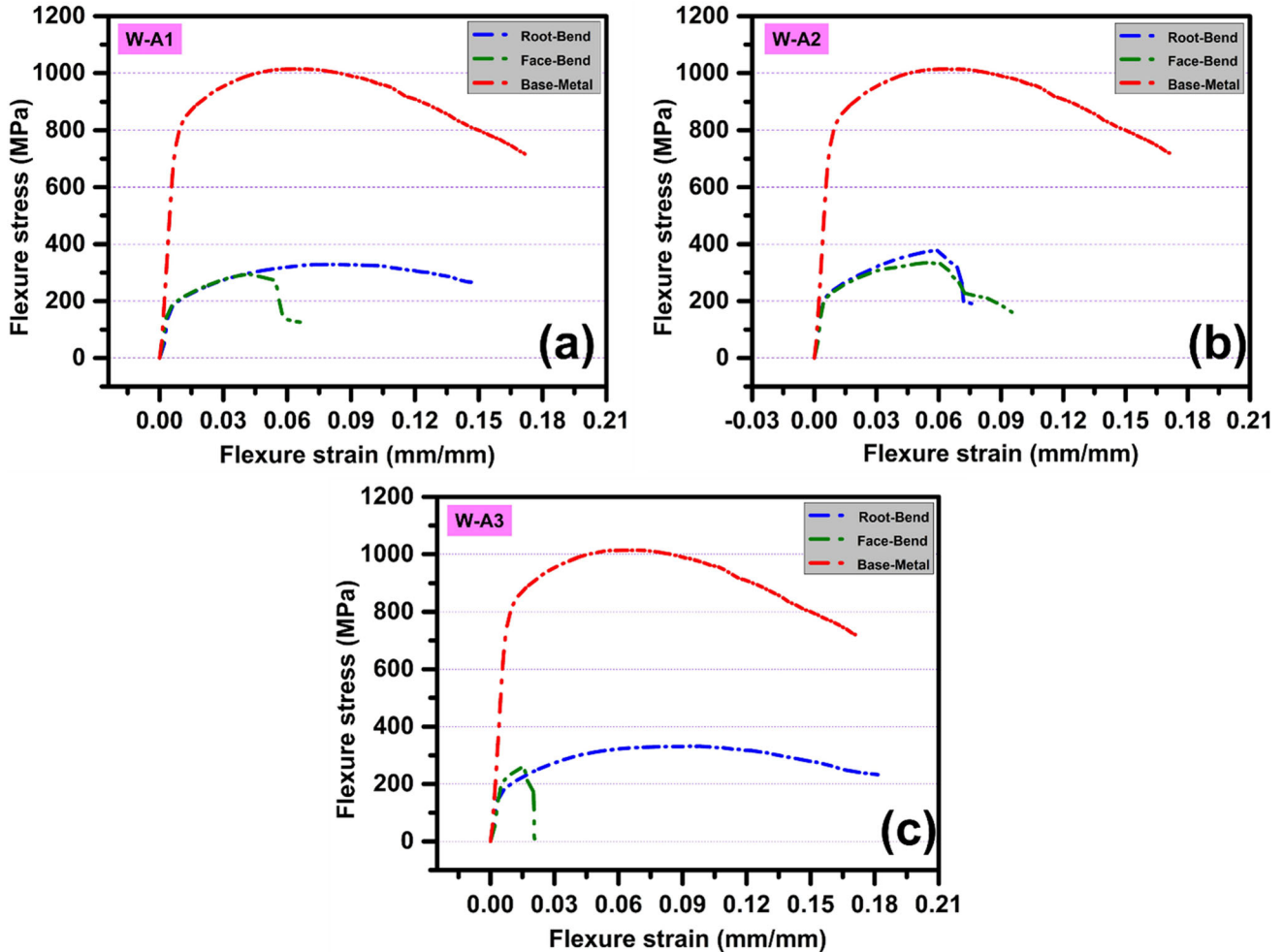


Fig. 11 Flexural strength (root and face bend) variation: (a) W-A1, (b) W-A2, and (c) W-A3

These results occur because of the existence of more plastic deformation and strain caused by the tool, resulting in a significant refining effect (Ref 53, 54). Therefore, it seems that the majority of heat generation by friction is situated below the tool shoulder area (i.e. the SZ and TMAZ regions). At numerous places, an unexpected increase in hardness value was observed because of IMC particles. By keeping rotational speed higher, the high-heat input offers suitable conditions for the development of IMCs and gives them appropriate hardness.

3.2.4 Residual Stress Analysis. Residual stresses refer to the internal forces that persist within a material after all external forces have been removed. These forces arise from uneven deformation caused by various factors like mechanical, thermal, or microstructural changes, such as in the phase transformation process. The degree of tensile residual stress present at a particular point is influenced by the extent of compressive plastic deformation that took place during the heating process.

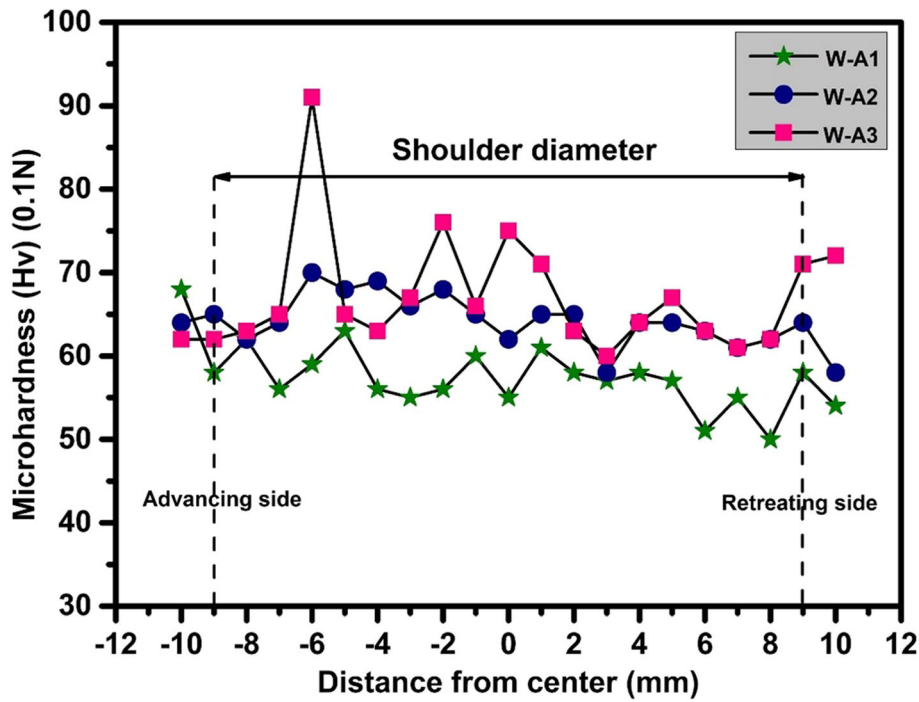


Fig. 12 Microhardness of FSW welds with rotational speed

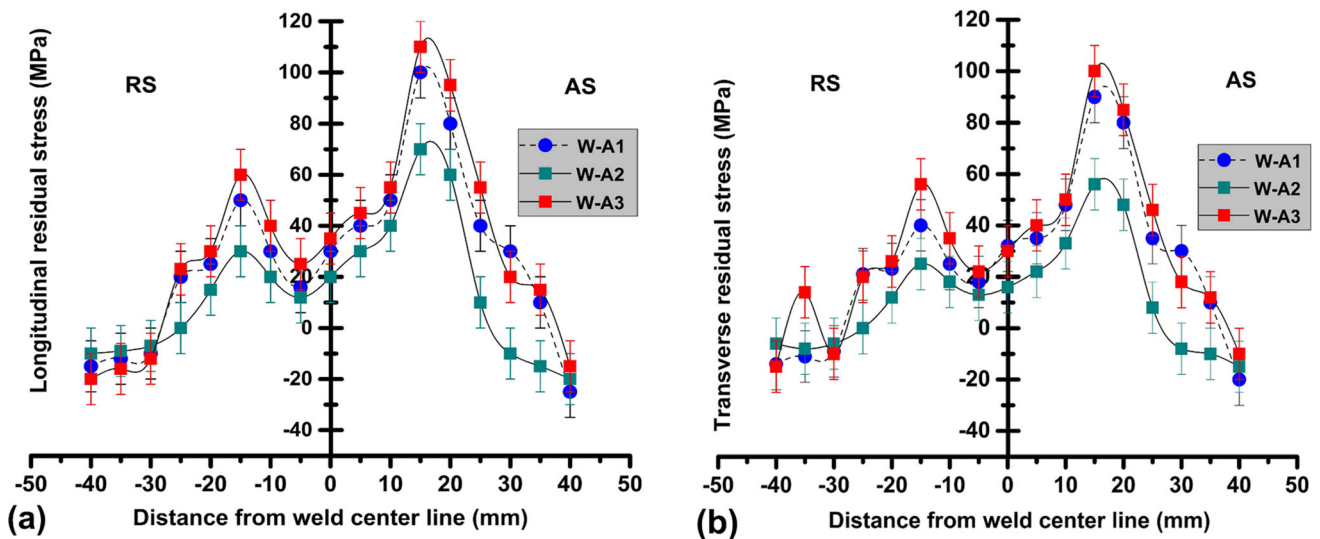


Fig. 13 Residual stress distribution of samples W-A1, W-A2 and W-A3 for (a) longitudinal residual stress, and (b) transverse residual stress

Regions located further from the weld zone edge will experience lower temperatures and less compressive stress, leading to less plastic deformation. Consequently, as you move away from the weld zone edge, the level of tensile residual stress will decrease.

The residual stress distribution in samples welded using different levels of heat input, namely W-A1, W-A2, and W-A3, is depicted in Fig. 13(a) and (b). The longitudinal residual stress on the advancing and retreating sides of samples W-A1, W-A2, and W-A3 is shown in Fig. 13(a), and it has a tensile nature.

The residual stress becomes maximum near the tool edge, which is tensile in nature, and then becomes minimum and ends up compressive as it goes away from the weld centre. The transverse residual stress behaves similarly to the longitudinal residual stress, but it has a compressive nature in the centreline of the weld (as shown in Fig. 13b). Moreover, the maximum residual stress in the transverse direction is quite below the longitudinal stress.

The residual stress distribution in the transverse and longitudinal directions is somewhat symmetrical. The highest

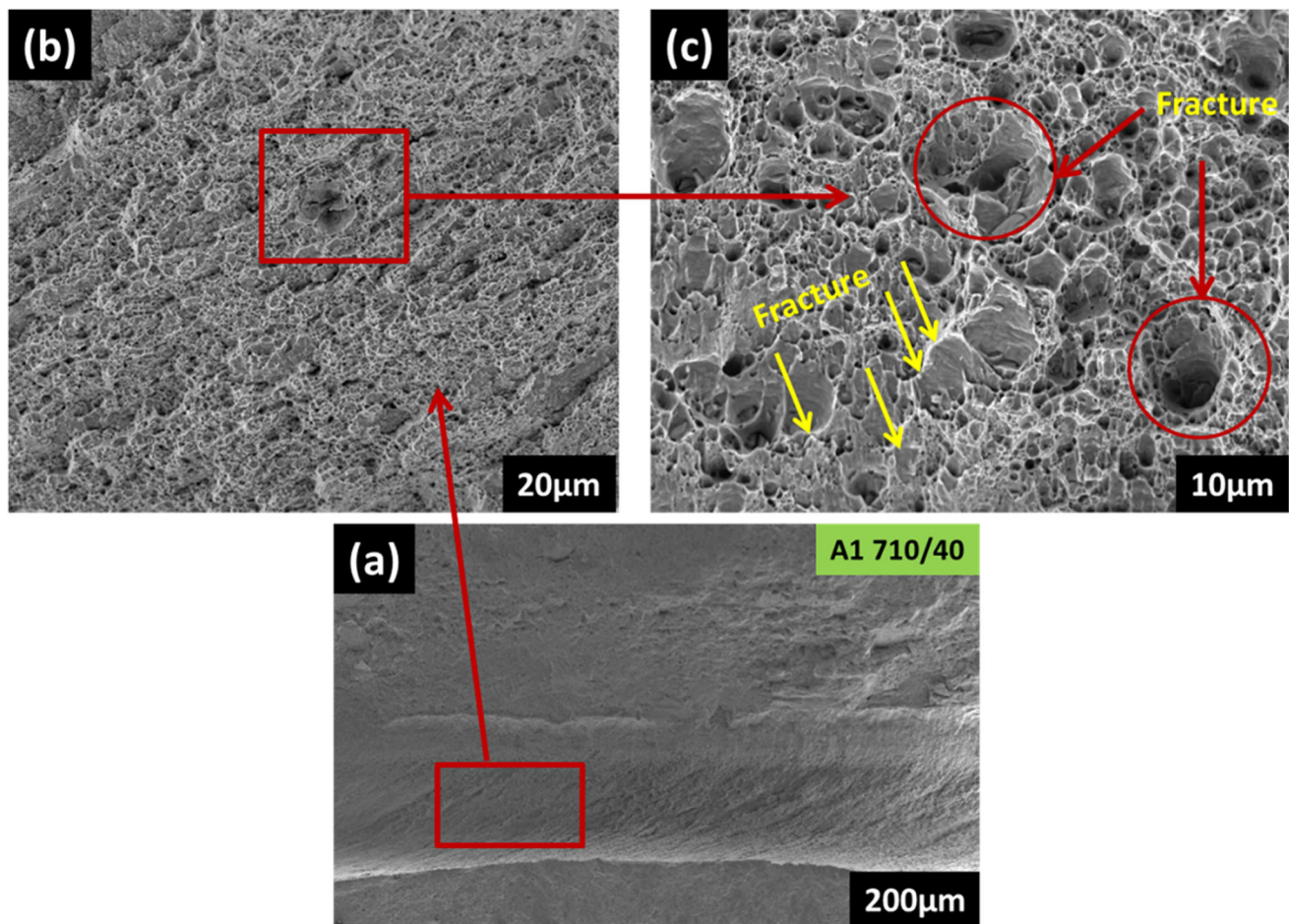


Fig. 14 Microstructure of fracture surface of sample W-A1

tensile residual stress is found on the advancing side of the weld. In addition to this, a significant finding (as depicted in Fig. 13) is that as the welding heat input increases (by increasing the rotational speed), the highest tensile residual stress and the tensile residual stress area size on both sides (advancing and retreating side) also increase, except for sample W-A2. For instance, in samples W-A1, W-A2, and W-A3, the highest tensile residual stresses on the advancing and retreating sides of the welds are 100, 70, and 110 MPa, respectively. Additionally, in samples W-A1, W-A2, and W-A3, the tensile residual stress area size is 60, 50, and 62 mm, respectively (as shown in Fig. 13a).

It can be observed that the distribution of residual stress on the advancing and retreating sides of the HAZ region is a function of the local mechanical characteristics and the varying inhomogeneous distribution of temperature post- and during the welding. Particularly, the HAZ, TMAZ, and SZ of the retreating side with a lesser residual stress distribution (as shown in Fig. 13a and b) also exhibit lower microhardness compared to the regions of the advancing side (as shown in Fig. 12). This is because the moderate heat input on the retreating side results in lower residual stress buildup compared to the advancing side. To put it briefly, the significant residual

tensile stress that happens near the weld is caused by an uneven distribution in the way thermal strain is managed whilst being heated and cooled.

3.3 Fracture Analysis

To compare the fracture behaviour of FSWed samples, W-A1, W-A2, and W-A3 were selected for fractography analysis. Typical SEM fractography of the tensile fracture of AA6061-T6 is shown in Fig. 14, 15 and 16. In the case of the low heat generation joint (i.e. W-A1, W-A2), the fracture surface had a dimple appearance characteristic, thus evidencing a ductile behaviour of failure. Whereas, in the case of the high-heat generation weld (i.e. W-A3), lesser dimples were noticeable; moreover, the original elongated contour grains can be recognised. A “river pattern” of radiating shapes is resulted by a mechanism known as cleavage and is typical characterised by a brittle fracture mechanism shown in Fig. 16(b) and (c). The fracture surface displays dimples, cleavage, and crack formation near the grain boundaries, which show the presence of both brittle and ductile natures of the fracture. Ductile fractures are considered to have enormous plastic deformation in advance of fracture compared to brittle fractures.

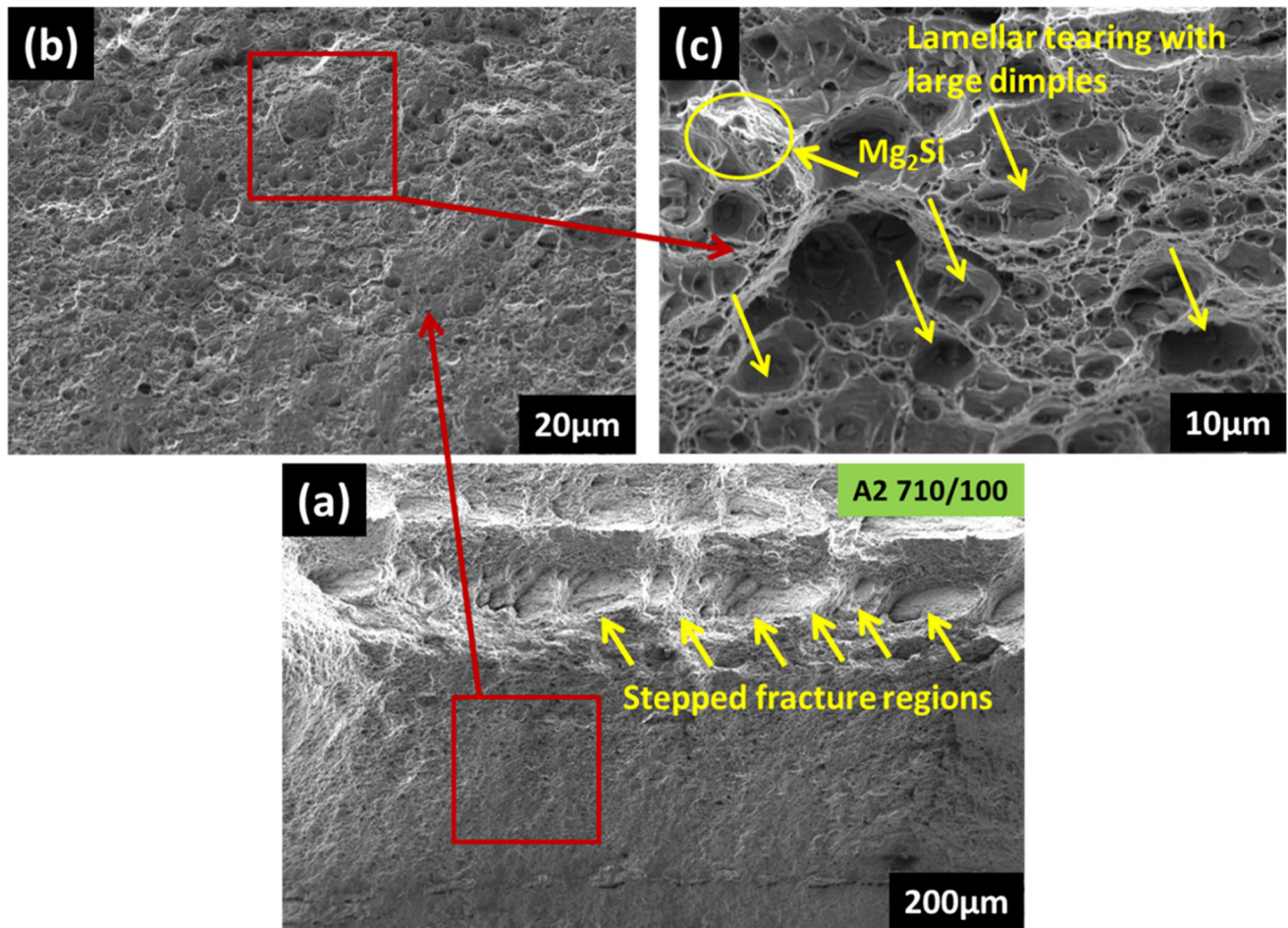


Fig. 15 Microstructure of fracture surface of sample W-A2

The development of dimples at lower rotational speeds, i.e. W-A1 and W-A2, was larger and occupied less area as compared to the dimples formed at higher rotational speeds, i.e. W-A3 (as shown in Fig. 16a, b, and c), because of better mechanical mixing of plasticized materials (Ref 37, 41, 46, 55). It was observed that during the tension test, the sample undergoes diffuse necking followed by local necking. In all cases, various dimples were scattered throughout the fracture surface, showing the ductile nature of the fracture.

4. Conclusions

The effect of linear speed and rotational speed on residual stress, mechanical properties, and microstructure of similar FSWed AA6061-T6 is studied by scanning electron microscopy (SEM), optical microscopy, microhardness, tensile, flexural, and XRD-based residual stress analysis. The findings can be expressed concisely in the following manner:

- XRD results revealed that Mg_2Si , Mg_5Si_6 , $MgZn_2$, $MgCu_2$, and Al_2CuMg IMCs were formed in various re-

gions, whereas β (Mg_2Si) and β'' (Mg_5Si_6) were found in Si-rich zones and offered favourable conditions for the metallurgical tuning and enhanced the mechanical performances.

- A defect-free joint was obtained for all cases, and the maximum tensile strength of 198 MPa was obtained for sample W-A2 in moderate heat conditions. Proper material mixing and heat input are key factors in enhancing tensile strength. The maximum mechanical joint efficiency with respect to base metal is 84.25%, obtained for sample W-A2, whereas the minimum is for sample W-A1, i.e. 72.77%. Grain size distribution is least for sample W-A2 due to proper stirring, whereas it is minimum for sample W-A1 due to inadequate heat input and improper stirring.
- The joint showed significant plastic deformation, and no surface cracks via the root-face-bend test were obtained for all sets of parameters. The maximum and minimum flexural strengths obtained during the root-bend test were 380 and 340 MPa for W-A2 and W-A1, respectively.
- The maximum value of hardness (i.e. 91 Hv) was observed in the HAZ of sample W-A3 on the advancing side, whereas the maximum microhardness for samples W-A2 and W-A1 was 70 and 61 Hv, respectively.

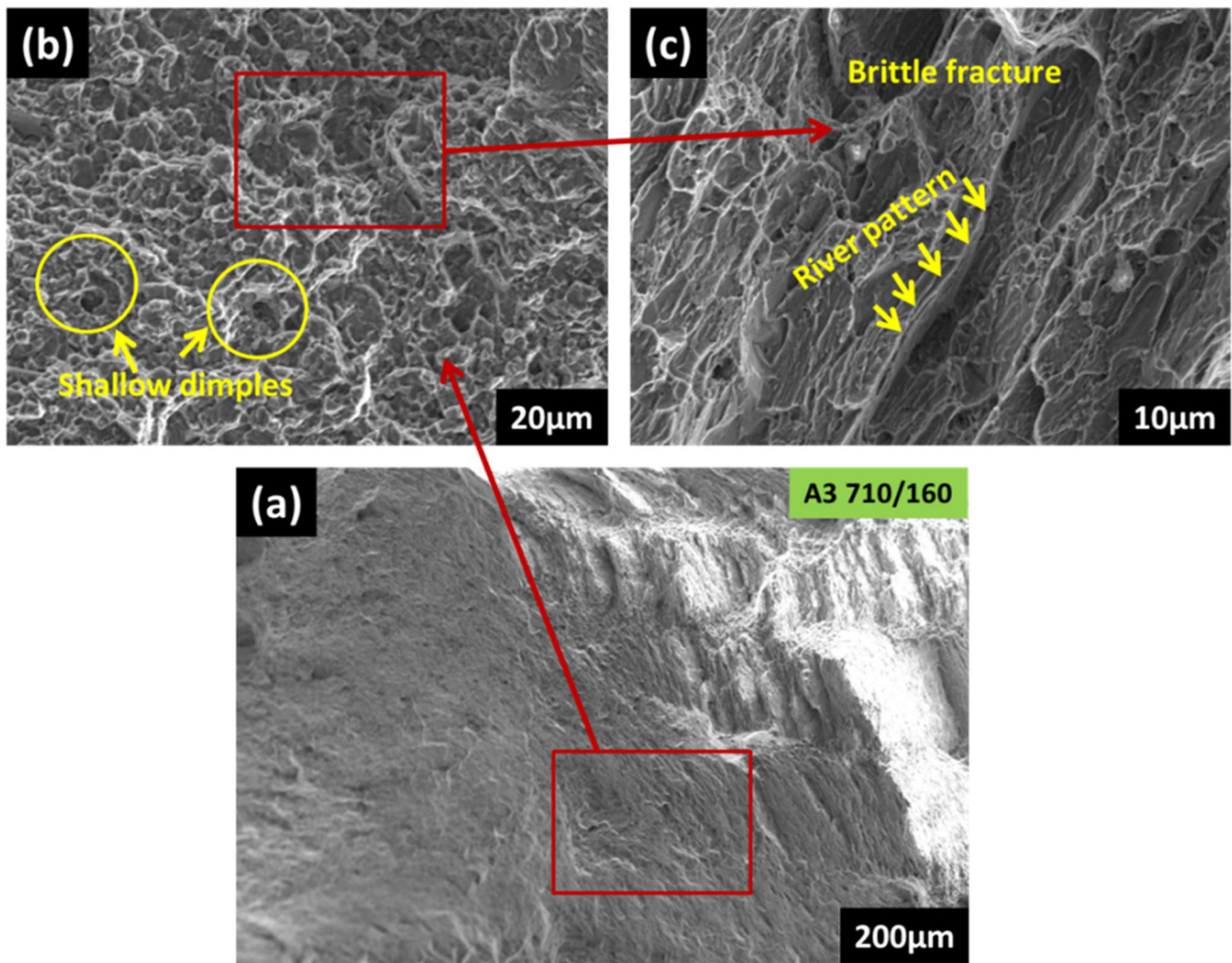


Fig. 16 Microstructure of fracture surface of sample W-A3

- The distribution of residual stress across various zones depends on the local mechanical characteristics and the temperature variations in different weld zones. When the welding heat input is increased, it leads to an increase in the maximum tensile residual stress.
- The longitudinal residual stress in the stir zone is predominantly tensile in nature, and moving away from the centre of the weld, it initially increases until reaching the highest tensile stress near the tool's edge. On the other hand, the transverse residual stress at the weld centre line is compressive in nature. Its maximum value is considerably lower compared to the longitudinal residual stress.

Funding

There is no funding for this research.

Conflict of interest

No conflict of interest.

References

1. A.L. Etter, T. Baudin, N. Fredj, and R. Penelle, Recrystallization Mechanisms in 5251 H14 and 5251 O Aluminum Friction Stir Welds, *Mater. Sci. Eng. A*, 2007, **445**, p 94–99
2. C. Du, X. Wang, Q. Pan, K. Xue, M. Ni, and J. Liu, Correlation Between Microstructure and Mechanical Properties of 6061–T6 Double-Side FSW Joint, *J. Manuf. Process.*, 2019, **38**, p 122–134
3. R.S. Mishra, and Z.Y. Ma, Friction Stir Welding and Processing, *Mater. Sci. Eng. R. Rep.*, 2005, **50**(1–2), p 1–78
4. T. Ding, H. Yan, J. Chen, W. Xia, B. Su., and H. Zhu, Microstructure Evolution and Recrystallization Mechanisms of High Mg Alloyed Al-Mg Alloy during Friction Stir Welding with Different Cooling Media. *J. Mater. Eng. Perform.*, 2022, p 1–12
5. J. Wang, B. Fu, L. Bergmann, F. Liu, and B. Klusemann, Effect of Welding Speed on Friction Stir Welds of PM2000 Alloy, *J. Mater. Eng. Perform.*, 2023, **32**(2), p 577–586
6. A.K. Kadian and P. Biswas, The Study of Material Flow Behaviour in Dissimilar Material FSW of AA6061 and Cu-B370 Alloys Plates, *J. Manuf. Process.*, 2018, **34**, p 96–105
7. S. Ravikumar, V.S. Rao, and R.V. Pranesh, Effect of Process Parameters on Mechanical Properties of Friction Stir Welded Dissimilar Materials Between AA6061-T651 and AA7075-T651 Alloys, *Int. J. Adv. Mech. Eng.*, 2014, **4**(1), p 101–114
8. M.M. Moradi, H.J. Aval, and R. Jamaati, Effect of Pre and Post Welding Heat Treatment in SiC-Fortified Dissimilar AA6061-AA2024 FSW Butt Joint, *J. Manuf. Process.*, 2017, **30**, p 97–105
9. J.F. Guo, H.C. Chen, C.N. Sun, G. Bi, Z. Sun, and J. Wei, Friction Stir Welding of Dissimilar Materials Between AA6061 and AA7075 Al

- Alloys Effects of Process Parameters, *Mater. Des.*, 2014, **1980–2015**(56), p 185–192
10. Y. Ni, L. Fu, Z. Shen, and X.C. Liu, Role of Tool Design on Thermal Cycling and Mechanical Properties of a High-Speed Micro Friction Stir Welded 7075–T6 Aluminum Alloy, *J. Manuf. Process.*, 2019, **48**, p 145–153
 11. P. Talebizadehsardari, F. Musharavati, A. Khan, T.A. Sebaey, A. Eyvaziana, and H.A. Derazkola, Underwater Friction Stir Welding of Al-Mg Alloy: Thermo-Mechanical Modeling and Validation, *Mater. Today Commun.*, 2021, **26**, p 101965
 12. A. Tavassolimanesh and A.A. Nia, A New Approach for Manufacturing Copper-Clad Aluminum Bimetallic Tubes by Friction Stir Welding (FSW), *J. Manuf. Process.*, 2017, **30**, p 374–384
 13. S.W. Williams and A. Steuwer, Residual stresses in friction stir welding. In *Friction Stir Welding*. Woodhead Publishing. 2010 p 215–244
 14. M. Kotobi and M. Honarposh, Experimental and Numerical Investigation of Through-Thickness Residual Stress of Laser-Bent Ti Samples, *J. Strain Anal. Eng. Des.*, 2017, **52**(6), p 347–355
 15. M. Honarposh, E. Haghghat, and M. Kotobi, Investigation of Residual Stress and Mechanical Properties of Equal Channel Angular Rolled St12 Strips, *Proc. Inst. Mech. Eng. Part L: J. Mater. Des. Appl.*, 2018, **232**(10), p 841–851
 16. M. Honarposh and H. Khanlari, A Numerical Study on the Residual Stress Measurement Accuracy using Inverse Eigenstrain Method, *J. Stress Anal.*, 2018, **2**(2), p 1–10
 17. F. Nazari, M. Honarposh, and H. Zhao, Effect of Stress Relief Annealing on Microstructure, Mechanical Properties, and Residual Stress of a Copper Sheet in the Constrained Groove Pressing Process, *Int. J. Adv. Manuf. Technol.*, 2019, **102**, p 4361–4370
 18. M. Sedighi and M. Honarposh, Experimental Study of Through-Depth Residual Stress in Explosive Welded Al–Cu–Al Multilayer, *Mater. Des.*, 2012, **37**, p 577–581
 19. M. Sedighi and M. Honarposh, Investigation of Cold Rolling Influence on Near Surface Residual Stress Distribution in Explosive Welded Multilayer, *Strength Mater.*, 2012, **44**, p 693–698
 20. M.S. Węglowski, P. Sedek, and C. Hamilton, Experimental Analysis of Residual Stress in Friction Stir Processed Cast AlSi9Mg Aluminium Alloy, *Key Eng. Mater.*, 2016, **682**, p 18–23
 21. C. Hamilton, M.S. Węglowski, S. Dymek, and P. Sedek, Using a Coupled Thermal/Material Flow Model to Predict Residual Stress in Friction Stir Processed AlMg9Si, *J. Mater. Eng. Perform.*, 2015, **24**, p 1305–1312
 22. N. Zhu, D.Z. Avery, Y. Chen, K. An, J.B. Jordon, P.G. Allison, and L.N. Brewer, Residual Stress Distributions in AA6061 Material Produced by Additive Friction Stir Deposition. *J. Mater. Eng. Perform.* 2022, p 1–10
 23. A. Tognan, L. Sandnes, G. Totis, M. Sortino, F. Berto, Ø. Grong, and E. Salvati, Evaluation and Origin of Residual Stress in Hybrid Metal and Extrusion Bonding and Comparison with Friction Stir Welding, *Int. J. Mech. Sci.*, 2022, **218**, p 107089
 24. I. Alinaghian, S. Amini, and M. Honarposh, Residual Stress, Tensile Strength, and Macrostructure Investigations on Ultrasonic Assisted Friction Stir Welding of AA 6061–T6, *J. Strain Anal. Eng. Des.*, 2018, **53**(7), p 494–503
 25. C. Dalle Donne, E. Lima, J. Wegener, A. Pyzalla, T. Buslaps, Investigations on Residual Stresses in Friction Stir Welds, in 3rd International Symposium on Friction Stir Welding 2001; Vol. 27
 26. Y.E. Ma, P. Staron, T. Fischer, and P.E. Irving, Size Effects on Residual Stress and Fatigue Crack Growth in Friction Stir Welded 2195–T8 Aluminium—Part I: Experiments, *Int. J. Fatigue*, 2011, **33**(11), p 1417–1425
 27. K.K. Kumar, A. Kumar, and M.V.N.V. Satyanarayana, Effect of Friction stir Welding Parameters on the Material flow, Mechanical Properties and Corrosion Behavior of Dissimilar AA5083-AA6061 Joints, *Proc. Inst. Mech. Eng. C J. Mech. Eng. Sci.*, 2022, **236**(6), p 2901–2917
 28. J. Dong, D. Zhang, W. Zhang, G. Cao, and C. Qiu, Effect of Post-Weld Heat Treatments on the Microstructure and Mechanical Properties of Underwater Friction Stir Welded Joints of 7003–T4/6060–T4 Aluminium Alloys, *Mater. Sci. Eng., A*, 2023, **862**, p 144423
 29. K.K. Kumar, A. Kumar, and S. Sundar, Investigation of Microstructure Characteristics and Work Hardening Behaviour of Water-Cooled FSW Dissimilar Aluminium Alloys, *Mater. Today Commun.*, 2023, **35**, p 105857
 30. K. Elangovan, V. Balasubramanian, and S. Babu, Predicting Tensile Strength of Friction Stir Welded AA6061 Aluminium Alloy Joints by a Mathematical Model, *Mater. Des.*, 2009, **30**(1), p 188–193
 31. F.J. Humphreys, A Unified Theory of Recovery, Recrystallization and Grain Growth, Based on the Stability and Growth of Cellular Microstructures—I. The Basic Model, *Acta Mater.*, 1997, **45**(10), p 4231–4240
 32. F.J. Humphreys, A Unified Theory of Recovery, Recrystallization and Grain Growth, Based on the Stability and Growth of Cellular Microstructures—II. The Effect of Second-Phase Particles, *Acta Mater.*, 1997, **45**(12), p 5031–5039
 33. K.A. Hassan, A.F. Norman, D.A. Price, and P.B. Prangnell, Stability of Nugget Zone Grain Structures in High Strength Al-Alloy Friction Stir Welds during Solution Treatment, *Acta Mater.*, 2003, **51**(7), p 1923–1936
 34. U.F.H.R. Suhuddin, S. Mironov, Y.S. Sato, H. Kokawa, and C.W. Lee, Grain Structure Evolution during Friction-Stir Welding of AZ31 Magnesium Alloy, *Acta Mater.*, 2009, **57**(18), p 5406–5418
 35. R. Dubey, R. Jayaganthan, D. Ruan, N.K. Gupta, N. Jones, and R. Velmurugan, (2022). Energy Absorption and Dynamic Behaviour of 6xxx Series Aluminium Alloys: A review. *Int. J. Impact Eng.*, 2022, p 104397
 36. V.P. Singh, S.K. Patel, A. Ranjan, and B. Kuriachen, Recent Research Progress in Solid State Friction-Stir Welding of Aluminium–Magnesium Alloys: A Critical Review, *J. Market. Res.*, 2020, **9**(3), p 6217–6256
 37. V.P. Singh, S.K. Patel, N. Kumar, and B. Kuriachen, Parametric Effect on Dissimilar Friction Stir Welded Steel-Magnesium Alloys Joints: A Review, *Sci. Technol. Weld. Join.*, 2019, **24**, p 653–684
 38. C.H.E.N. Yu, D.I.N.G. Hua, J.Z. Li, J.W. Zhao, M.J. Fu, and X.H. Li, Effect of Welding Heat Input and post-Welded Heat Treatment on Hardness of Stir Zone for Friction Stir-Welded 2024–T3 Aluminum Alloy, *Trans. Nonferr. Metals Soc. China*, 2015, **25**(8), p 2524–2532
 39. C. Leitao, R.M. Leal, D.M. Rodrigues, A. Loureiro, and P. Vilaça, Mechanical Behaviour of Similar and Dissimilar AA5182-H111 and AA6016-T4 Thin Friction Stir Welds, *Mater. Des.*, 2009, **30**(1), p 101–108
 40. M. Paidar, A. Khodabandeh, H. Najafi, and A.S. Rouh-aghdam, Effects of the Tool Rotational Speed and Shoulder Penetration Depth on Mechanical Properties and Failure Modes of Friction Stir Spot Welds of Aluminum 2024–T3 Sheets, *J. Mech. Sci. Technol.*, 2014, **28**, p 4893–4898
 41. V.P. Singh, S.K. Patel, and B. Kuriachen, Mechanical and Microstructural Properties Evolutions of Various Alloys Welded Through Cooling Assisted Friction-Stir Welding: A Review, *Intermetallics*, 2021, **133**, p 107122
 42. V.P. Singh and B. Kuriachen, Experimental Investigations Into the Mechanical and Metallurgical Characteristics of Friction Stir Welded AZ31 Magnesium Alloy. *J. Mater. Eng. Perform.* 2022, p 1–17
 43. V.P. Singh, D. Kumar, R.P. Mahto, and B. Kuriachen, Microstructural and Mechanical Behavior of Friction-Stir-Welded AA6061-T6 and AZ31 Alloys with Improved Electrochemical Corrosion, *J. Mater. Eng. Perform.*, 2023, **32**(9), p 4185–4204
 44. B. Kulkarni, S. Pankade, S. Tayde, and S. Bhosle, Corrosion and Mechanical Aspects of Friction Stir Welded AA6061 joints: Effects of Different Backing Plates, *J. Mater. Eng. Perform.*, 2023 <https://doi.org/10.1007/s11665-023-07900-x>
 45. P. Prakash, R.S. Anand, and S.K. Jha, Experimental Analysis of Tensile Strength of Different Thicknesses and Dissimilar Aluminum Alloys in Friction Stir Welding, *J. Mater. Eng. Perform.*, 2022 <https://doi.org/10.1007/s11665-022-07694-4>
 46. W. Xu, J. Liu, G. Luan, and C. Dong, Microstructure and Mechanical Properties of Friction Stir Welded Joints in 2219–T6 Aluminum Alloy, *Mater. Des.*, 2009, **30**(9), p 3460–3467
 47. K. Dehghani, R. Ghorbani, and A.R. Soltanipoor, Microstructural Evolution and Mechanical Properties during the Friction Stir Welding of 7075-O Aluminum Alloy, *Int. J. Adv. Manufact. Technol.*, 2015, **77**, p 1671–1679
 48. L.I. Tian, D.W. Zhou, Y.A.N. You-rui-ling, P.E.N.G. Ping, and J.S. Liu, First-principles and Experimental Investigations on Ductility/Brittleness of Intermetallic Compounds and Joint Properties in Steel/

- Aluminum Laser Welding, *Trans. Nonferr. Metals Soc. China*, 2021, **31**(10), p 2962–2977
49. V. Msomi and N. Mbona, Mechanical Properties of Friction Stir Welded AA1050-H14 and AA5083-H111 Joint: Sampling Aspect, *Metals*, 2020, **10**(2), p 214
 50. H.I. Dawood, K.S. Mohammed, A. Rahmat, and M.B. Uday, The Influence of the Surface Roughness on the Microstructures and Mechanical Properties of 6061 Aluminium Alloy using Friction Stir Welding, *Surf. Coat. Technol.*, 2015, **270**, p 272–283
 51. A. Scialpi, M. De Giorgi, L.A.C. De Filippis, R. Nobile, and F.W. Panella, Mechanical Analysis of Ultra-Thin Friction Stir Welding Joined Sheets with Dissimilar and Similar Materials, *Mater. Des.*, 2008, **29**(5), p 928–936
 52. P.M.G.P. Moreira, T. Santos, S.M.O. Tavares, V. Richter-Trummer, P. Vilaça, and P.M.S.T. De Castro, Mechanical and Metallurgical Characterization of Friction Stir Welding Joints of AA6061-T6 with AA6082-T6, *Mater. Des.*, 2009, **30**(1), p 180–187
 53. T. Hirata, T. Oguri, H. Hagino, T. Tanaka, S.W. Chung, Y. Takigawa, and K. Higashi, Influence of Friction Stir Welding Parameters on Grain Size and Formability in 5083 Aluminum Alloy, *Mater. Sci. Eng., A*, 2007, **456**(1–2), p 344–349
 54. G.R. Babu, K.G.K. Murthi, and G.R. Janardhana, An Experimental Study on the Effect of Welding Parameters on Mechanical and Microstructural Properties of AA 6082–T6 Friction Stir Welded Butt Joints, *ARPN J. Eng. Appl. Sci.*, 2008, **3**(5), p 68–73
 55. G. Madhusudhan Reddy, P. Mastanaiah, K. Sata Prasad, and T. Mohandas, Microstructure and Mechanical Property Correlations in AA 6061 Aluminium Alloy Friction Stir Welds, *Trans. Indian Inst. Met.*, 2009, **62**, p 49–58

Publisher's Note Springer Nature remains neutral with regard to jurisdictional claims in published maps and institutional affiliations.

Springer Nature or its licensor (e.g. a society or other partner) holds exclusive rights to this article under a publishing agreement with the author(s) or other rightsholder(s); author self-archiving of the accepted manuscript version of this article is solely governed by the terms of such publishing agreement and applicable law.